Preparation and Characterization of Novel Polyvinyl Alcohol-Alginate Beads for Quorum Quenching Application in Membrane Bioreactors

Ermias Mideksa, Johanne Teychene, Valerie Sartor, Catherine Claparols, Christelle Guigui, Audrey Tourrette

Preparation and Characterization of Novel Polyvinyl Alcohol-Alginate Beads for Quorum Quenching Application in Membrane Bioreactors

Ermias Mideksa[1,2], Johanne Teychene[1*], Valerie Sartor[3], Catherine Claparols[4], Christelle Guigui[1], Audrey Tourrette[2]

***Corresponding authors:** Johanne Teychene (rumpala@insa-toulouse.fr)
***ORCID ID**: https://orcid.org/0000-0002-2997-4744

1. TBI, INSA, CNRS UMR 5504, INRA UMR 792, Université de Toulouse, 31077 Toulouse, France
2. CIRIMAT, Université Toulouse III – Paul Sabatier, Toulouse INP, CNRS, Université de Toulouse, 31062 Toulouse, France
3. Laboratoire Softmat, CNRS UMR 5623, Université Toulouse III – Paul Sabatier, 31077 Toulouse, France
4. LCC-CNRS, Université Toulouse III – Paul Sabatier, 31077 Toulouse, France

Highlights

- Detailed preparation and characterization of new PVA-Alginate beads for Quorum Quenching application.
- Supercritical CO_2 (SC-CO_2) drying proved a reliable bead drying technique.
- Beads' pore structure was modified by changing the composition of the crosslinking solution.
- Beads with finger-like pores show superior AHL incorporation capacity compared to other bead types.

Graphical abstract

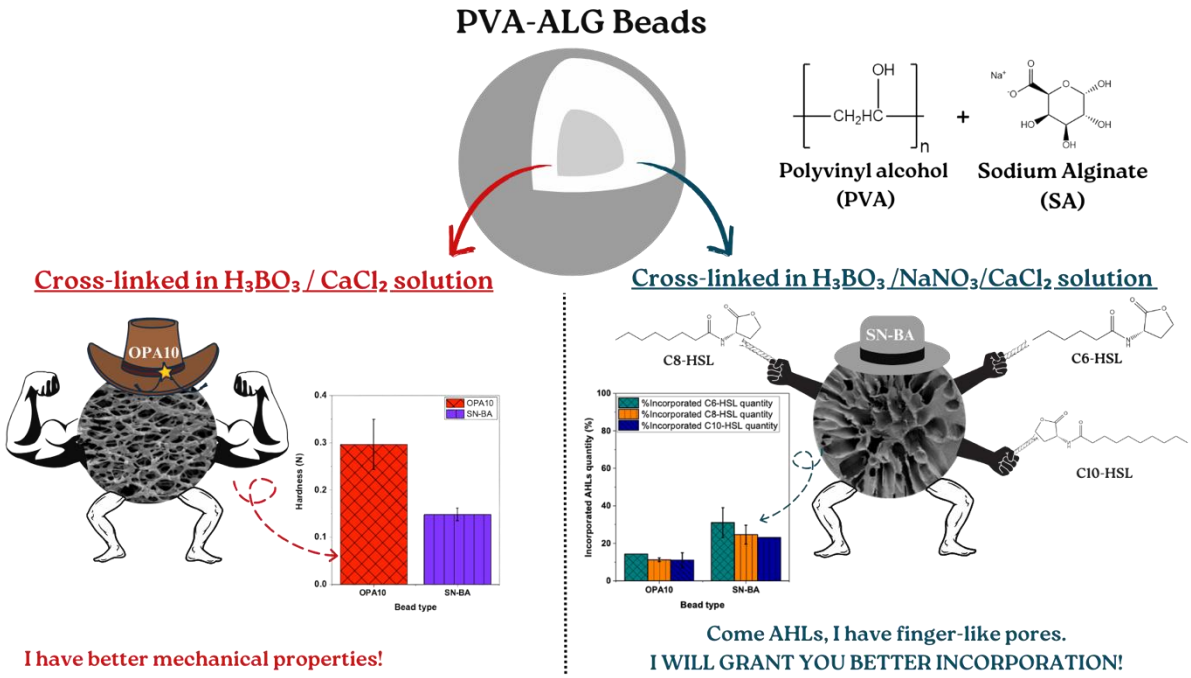

Abstract

Quorum quenching (QQ) has emerged as an effective biofouling mitigation approach in membrane bioreactors. This study presents new approaches for preparing and characterizing polyvinyl alcohol (PVA) and alginate beads for QQ applications. The effects of change in concentration of PVA, crosslinking solution composition, and the impact of mixture dissolution method on physicochemical, acyl homoserine lactones (AHLs) incorporation and mechanical properties were investigated. Comparisons between evaporative, freeze, and supercritical CO_2 drying techniques were followed to characterize textural and structural properties. Beads' structure, mechanical, chemical modification, and textural properties were characterized by scanning electron microscopy, texture profile analysis, Nitrogen physisorption, and attenuated total reflection Fourier transform infrared spectroscopy analysis. Changes in the concentration of PVA and mixture dissolution method impact the bead pore structure, swelling properties, and AHL incorporation. Changes in the composition of the primary crosslinking solution cause modifications in the beads' chain and pore structure. Beads crosslinked using a primary crosslinking solution composed of boric acid and calcium chloride possess internal structures with high chain interconnection and hardness. Meanwhile, beads prepared by blending the boric acid and calcium chloride's primary crosslinking solution with sodium nitrate (named SN-BA) provided new bead types with pores resembling fingers. Nitrogen physisorption analysis revealed the beads have a surface area between 16 m^2/g and 23 m^2/g with dominating mesopores. The finger-like pores enhanced the AHL permeation compared to beads with interconnected polymer chains. SN-BA beads incorporated around 30% of C6-HSL, 24% of C8-HSL, and 23% of C10-HSL.

Keywords: Quorum Quenching, PVA-Alginate beads, Finger-like pores, Supercritical CO_2 drying, AHLs incorporation capacity

1. Introduction

Membrane bioreactors (MBRs) are recognized as efficient technology for industrial and municipal wastewater treatment [1]. MBRs utilize a biological reactor coupled with a filtration membrane for wastewater purification. Nevertheless, membrane biofouling, characterized by a biofilm formation and deposition on filtration membrane, still poses a significant challenge [2, 3]. Membrane biofouling has been reported to be tightly linked to Quorum Sensing (QS), a bacterial cell-to-cell communication that results in the production of extracellular polymeric substances (EPS), which are the main components of biofilms in MBR [1–5]. QS allows bacteria to control gene expression in response to population density [6]. When their concentration attains a threshold level, it combines with the receptor protein and activates the transcription of specific genes to induce group behaviors such as biofilm formation [3, 6–8]. Signal molecules identified to date are mainly N-acyl-L-homoserine lactones (AHLs) for gram-negative and autoinducing peptides (AIPs) for gram-positive bacteria. Furanosyl borate diesters and AI-2 signals are used for interspecies communication [3, 9]. In MBRs, the most prevalent bacterial communication, causing membrane biofouling, is due to AHLs secreted from the dominant gram-negative bacteria in wastewater [10, 11]. Quorum Quenching (QQ) recently emerged as a biofouling control approach to disrupt QS. QQ centers on QS inhibition by degrading AHLs using the enzyme-secreting QQ-bacteria like *Rhodococcus sp*.BH4 and *Pseudomonas sp.*1A1 [10, 12].

To ensure effective inhibition of QS by QQ-bacteria, encapsulation of these bacteria within a QQ-media is crucial. Encapsulation shields the QQ-bacteria from harsh environments in wastewater, like bacteriophages, and varying pH, temperature, and hydrodynamic conditions to enhance their vitality and efficacy over extended operation periods [1, 13]. Above all, QQ-media provides a suitable habitat for bacterial colonization, attachment, and nutrient supply [14]. Mobile QQ media like QQ-beads, hollow cylinders, and QQ sheets are considerably effective in biofouling mitigation due to the frequent contact of the media with wastewater, which improves the mass transfer [3,10]. The frequent collision of mobile QQ-medias with the filtration membrane enhances biofilm detachment in conjunction with AHL degradation by QQ-bacteria [16]. Of all the mentioned mobile QQ media, QQ-beads are common due to their relative ease of preparation compared to hollow cylinders and sheets [17]. Hydrogel-based QQ bacteria cell entrapping beads (CEBs) composed of only Sodium Alginate (SA) were first introduced by Kim et al. [4]. QQ-CEBs showed promising biofouling control in MBRs for less than 30 days. They also demonstrated QQ-activity, as they effectively degraded C8-HSL, an abundant AHL in biofilm-formed MBRs [4]. Despite these advantages, SA beads were reported to have poor chemical and mechanical stability as they are susceptible to change with pH and structural decomposition when introduced to MBRs with real wastewater [18]. To reinforce beads' mechanical stability, the preparation of chemically crosslinked QQ-beads mainly composed of polyvinyl alcohol (PVA) and SA was first introduced by Lee et al. [18]. In PVA-Alginate (ALG) beads, a small amount of SA is added to improve the surface properties of PVA by inducing steric and electrostatic stabilization effects and preventing bead agglomeration during the crosslinking process [19]. QQ-beads composed of PVA and SA showed enhanced biofouling control for > 100 days without showing signs of decomposition compared to beads composed of only SA [18].

Chemical crosslinking of PVA and SA by using boric acid (H_3BO_3) and calcium chloride ($CaCl_2$) is the most common, easy, and cost-effective method to produce durable beads [17]. QQ-beads formed using only boric acid and calcium chloride crosslinking agents are not suitable for direct use in MBRs due to the reversible nature of the boric acid-PVA complex upon immersion in water, as reported by Zain et al. [20]. To solve this problem, followed this study reported a new approach to initially crosslink the PVA/SA mixture in a boric acid and calcium chloride solution and transfer to a secondary crosslinking solution composed of sodium sulfate. They proposed a nucleophilic substitution mechanism whereby the sulfate ions attack borate ions to replace them in a mechanism known as the Walden inversion, resulting in water-stable beads applicable for use in MBRs [20]. As mentioned, the crosslinking solutions used for QQ-bead preparation to date are composed of boric acid, calcium chloride, and sodium sulfate. The saturated boric acid solution used for crosslink PVA is quite acidic (pH = 4), which can cause difficulty maintaining bacteria viability [19]. Boric acid compromises cell viability by interfering with bacteria metabolism, disrupting cell membrane integrity, and inducing oxidative

stress, according to Wu et al. [19] and Candry et al. [21]. The ideal approach to replace boric acid is to use a crosslinking solution containing nucleophilic ions like sulfates, phosphate, and nitrates with calcium chloride with the ability to crosslink the PVA/SA mixture and provide water-stable beads in a single step [22]. However, this attempt poses a challenge as the beads face difficulty forming a stable structure due to the slow crosslinking rate. A potentially new and unexplored approach involves blending boric acid and calcium chloride solution with an additional crosslinking agent that crosslinks PVA concurrently but adjusts the crosslinking rate to create new types of beads with unique structural properties [21].

To ensure the effective degradation of AHLs by the QQ-bacteria in MBRs, tuning the physicochemical properties of beads is crucial. For example, in the case of encapsulating *Rhodococcus sp*. BH4, a QQ-bacteria that secretes an endo-enzyme, AHL degradation occurs in bacteria cells. It involves steps including diffusion of AHLs from the wastewater, adsorption, and internal diffusion of AHLs onto the beads. Then, enzymatic degradation of AHLs takes place inside the QQ-bacteria [3]. The physicochemical properties of the beads highly influence the diffusion and adsorption of AHLs into the beads, hence the overall efficiency of QQ [5, 23]. The beads' properties are influenced by a multitude of parameters, including the molecular weight of PVA, the degree of hydrolysis of PVA, pH, crosslinking time, and the type of crosslinking solution used [15, 21, 24]. The PVA-to-SA ratio is one of the most critical parameters that dictate their physicochemical properties, immensely influencing the resulting beads' structure, texture, and mechanical properties. Preparation of QQ-beads primarily adopts PVA-ALG concentration reported by Lee et al. [18], where the polymer mixture is composed of a 10:1 ratio of PVA and SA. Nevertheless, Islam et al. [17] took a slightly different approach, forming beads with 8% w/v PVA and 1% w/v SA, utilizing PVA with a degree of polymerization close to that reported by Lee. Despite existing research on the fabrication of PVA-ALG beads, a study to date has yet to explore the effect of change in PVA and SA composition, mainly the concentration of PVA, in relation with the structural, textural properties and AHL incorporation capacity of beads. Additionally, the method employed to dissolve the polymer mixture is very crucial. Several studies reported the effect of ultrasonic dissolution (US) on the polymer mixture homogeneity, exposure of polymer functional groups, molecular weight modification, distinct mechanical properties, and the moisture absorption capacity of PVA films and other hydrophilic polymers [25–30]. Given these findings, we found it essential to investigate how ultrasonic dissolution affects the physicochemical properties of PVA-ALG beads compared to those prepared using polymer mixtures dissolved by traditional dissolution techniques, such as a dry heating oven.

Exploring the physicochemical properties of PVA-ALG beads is critical to understanding their structure and texture, revealing important details about the mechanical and swelling properties and ability to incorporate AHLs. However, the hydrated nature of PVA-ALG beads poses a significant challenge. The water inside interferes with instrumental techniques, making the characterization of physicochemical properties difficult [31, 32]. Considering this limitation, only a few studies have characterized the structural and textural properties of PVA-ALG beads. A study by Islam et al. [15] reported the structure of freeze-dried QQ beads. Even though this study unveiled the shape of the QQ-bacteria, the overall bead structure and pore morphology appeared severely altered. A study by Iqbal et al. [2] also successfully revealed the rod shape of *Rhodococcus sp*.BH4 on the QQ-sheet surface but not the pore morphology of the QQ media itself [10]. Apart from such attempts, studies have yet to provide a concrete strategy to characterize structural and textural properties like the porosity, pore size, and surface area of different PVA-ALG beads for QQ application. As mentioned, the hydrated nature of PVA-ALG beads poses a significant challenge to the characterization of physicochemical properties; thus, it is crucial to follow a drying technique before further characterization of the physicochemical properties. However, the drying method remains a sensitive step that can alter these properties [31, 32]. Selecting a drying technique that can preserve the beads' three-dimensional porous internal structure and texture is crucial. To face this challenge, a comparison of bead drying techniques like evaporative heat, freeze, and supercritical CO_2 (SC-CO_2) drying techniques is investigated.

Accordingly, this study presents follow-ups of novel strategies for preparing and characterizing vacant PVA-ALG beads (without QQ-bacteria). The effects of change in concentration of PVA, crosslinking solution composition, and the method of mixture dissolution on the physicochemical properties were examined. A detailed comparison between evaporative, freeze-drying, and SC-CO_2 drying techniques was made to understand

PVA-ALG beads' textural and structural properties. Ultimately, the mechanical property and the AHL incorporation capacity of the PVA-ALG beads were investigated by using texture profile and Ultrahigh-performance liquid chromatography coupled Mass spectrometry (UHPLC-MS/MS) analysis, respectively.

2. Materials and Methods

2.1 Chemicals

Polyvinyl alcohol (PVA) with a molecular weight of 88 to 98 kDa (98-100% hydrolyzed) was acquired from Alfa Aesar®, Germany. Medium viscosity Sodium Alginate (SA) was obtained from Sigma Aldrich®, UK. Other reagents, including Boric acid (H_3BO_3), Calcium chloride dihydrate ($CaCl_2{\cdot}2H_2O$), Sodium sulfate (Na_2SO_4), Sodium nitrate ($NaNO_3$), N-hexanoyl-L-homoserine lactone (C6-HSL), N-octanoyl-L-homoserine lactone (C8-HSL), N-decanoyl-L-homoserine lactone (C10-HSL), liquid chromatography-mass spectrometry (LC-MS) grade acetonitrile (CH_3CN), and formic acid (HCOOH), were purchased from Sigma Aldrich®, UK. Absolute Ethanol (C_2H_5OH) (> 99.8%) was purchased from Alfa Aesar®, Germany. All solutions were prepared using ultrapure water (conductivity ~ 0.06 µS/cm).

2.2 Preparation of vacant PVA-ALG beads

Several polymer mixtures of PVA and SA dissolved and crosslinked in different conditions were used to prepare vacant PVA-ALG beads (without QQ-bacteria). The preparation procedure of the PVA-ALG mixture and beads are summarized in Fig. 1 and Table 1. For procedure A (OPA10), a mixture of PVA-ALG was dissolved in a heating oven (Memmert UM100, Germany) with 10% w/v PVA and 1% w/v SA concentration. For preparation procedure B (US-10), the concentration of PVA and SA was kept the same as in procedure A. Then, the PVA/SA mixture was continuously swept in an ultrasonic water bath at 37 KHz and 600 W (Elmasonic® 60H, Germany). For procedure C (OPA8), the concentration of PVA was reduced to 8% w/v while keeping the SA concentration at 1 %w/v. This mixture was then dissolved in the heating oven. For procedure D (SN-BA), the mixture dissolved was dissolved in a heating oven with 10% w/v PVA and 1% w/v SA concentration. After preparing the respective polymer mixtures, the dissolved solutions were placed in a syringe pump (Harvard apparatus®, USA) and dropped at 500 $\mu L.min^{-1}$ into the first crosslinking solution, as shown in Fig. 1. For the polymer mixture mentioned from procedures A to C, the mixture was initially dropped into a primary crosslinking solution of boric acid (7% w/v) and calcium chloride (4% w/v) for 2 hours ± 10 min. The beads were then carefully rinsed with ultrapure water and transferred into a 0.5 M sodium sulfate solution for another 2 hours ± 10 min. The PVA/SA mixture was initially crosslinked for procedure D in a boric acid, sodium nitrate, and calcium chloride solution. The beads were then transferred into 0.5 M solution for 2 hours ± 10 min.

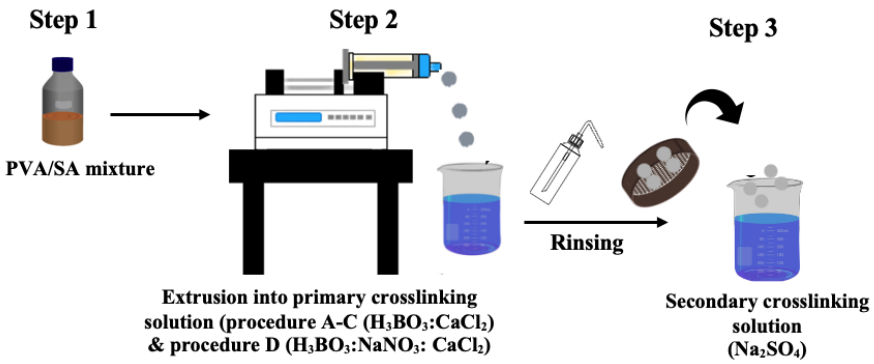

Fig. 1 Preparation of vacant PVA-ALG beads via the chemical crosslinking process

Table 1 Preparation procedure of PVA-ALG beads and different controlled parameters.

Procedure	Bead type	Step 1				Step 2		Step 3
		Concentration (%w/v)		Dissolution method	Temperature (^{0}C)	Primary crosslinking solution		Secondary crosslinking solution
		PVA	SA			H_3BO_3 and $CaCl_2$ (% w/v: %w/v)	$NaNO_3$ (% w/v)	Na_2SO_4 (M)
A	OPA10	10	1	Oven	90	7:4	-	0.5
B	US-10	10	1	Sonication	90	7:4	-	0.5
C	OPA8	8	1	Oven	105	7:4	-	0.5
D	SN-BA	10	1	Oven	90	5:4	2	0.5

2.3 Characterization of PVA/SA polymer mixtures

2.3.1 Viscosity

The Rheomat (RM180, Rheometric Scientific Inc, USA) rotational viscometer was used to measure the viscosity of all PVA-ALG mixtures at 25 ± 2 ^{0}C. The mixture was then introduced into a metal tube, and different shear rates were applied. Three separate PVA/SA mixtures and control solutions solely composed of either PVA or SA were prepared and analysed.

2.3.2 Surface tension

The surface tension measurements of PVA-ALG mixtures were obtained using a surface tensiometer (KRÜSS K6, Germany) equipped with a tungsten ring at 25 ± 2 ^{0}C. Five measurements were taken for each mixture type and averaged.

2.4 Characterization of dry PVA-ALG beads

2.4.1 Drying procedure

As reported in the literature, a proper drying procedure must be followed to evaluate hydrated PVA-ALG beads' porosity, specific surface area, and pore size [15, 31, 32]. Evaporative heat drying, freeze drying, and supercritical CO_2 drying techniques were evaluated to select the appropriate drying procedure.

a) Evaporative heat drying

The evaporative drying procedure was done in a heating oven where 5 grams of wet PVA-ALG beads were dried at 50^{0}C.

b) Freeze drying

The freeze-drying procedure was carried out by taking 5 grams of wet beads. The beads were frozen overnight and then freeze-dried (Labconco®, USA) at -50 ^{0}C and 2500 mbar.

c) Supercritical CO_2 drying

Wet PVA-ALG beads were initially dehydrated by immersion in consecutive ethanol baths with 10% v/v, 30% v/v, 50% v/v, and 80% v/v for fifteen minutes each. After, the beads were transferred into three separate baths containing absolute ethanol for the same duration. The beads were then consecutively washed with liquid CO_2 to replace the ethanol present within the beads completely. This was followed by drying the beads in supercritical

condition at 31.5 ^{0}C and 74 bars using Polaron 3100 [32]. The size of PVA-ALG beads was measured after the dehydration and SC-CO_2 drying steps to analyze their shrinkage from the initial wet state. The shrinkage (%) of the beads was then calculated using Equ. (1).

$$Shrinkage = \frac{V_w - V_d}{V_w} * 100 \quad (1)$$

Where V_w represents the volume of the wet beads, and V_d represents the volume of the beads after dehydration with ethanol and supercritical drying steps.

2.4.2 Nitrogen physisorption analysis

After selecting the proper drying procedure, the beads' adsorption-desorption isotherms were registered using Micromeritics Tri-Star II volumetric apparatus admitting doses of nitrogen gas in a measurement cell at 77 K. The beads were outgassed for 12 hours at 323 K until a 0.4 Pa stable vacuum was reached to remove any existing moisture. The specific surface area of PVA-ALG beads was evaluated using the Brunauer–Emmett–Teller (BET) method. The pore size and volume analysis were done from the desorption branch of the physisorption isotherm using both BJH and the DFT model considering the shape of the pores cylindrical. The shape of the nitrogen (N_2) physisorption isotherm provides information on the overall porosity of the beads [32]. For each bead type, the N_2 physisorption analysis was duplicated.

The net molar energy of adsorption (ΔE) is defined by the difference in the energy of adsorption (E_{ads}) and liquefication (5.6 KJ.mol^{-1} for N_2), representing the interaction between the first adsorbate layer ($E_{adsorbtion}$) and the following layers ($E_{liquification}$) with the bead surface. It was calculated using Equation (2) [31].

$$\Delta E = RTln(C - BET) \quad (2)$$

Where R= 8.3145 J.mol^{-1}. K^{-1}, T is the temperature at which nitrogen gas is admitted to the measurement cell in kelvin (K), and C - BET, which implies affinity strength between the adsorbate and surface of the beads is obtained experimentally.

2.4.3 Scanning Electron Microscopy (SEM)

The dry beads' surface and internal morphology were investigated using a scanning electron microscope (Quanta™ FEG 250, USA). The images were recorded using secondary electron detectors (SE). The acceleration voltage was set at 5 kV to prevent any beam-induced modifications. Dry beads were directly stuck on a stub for surface morphology observations. At the same time, the internal morphology was visualized using dried beads that were sliced during the dehydration step. These beads were coated with a 6 nm conductive platinum layer. Surface and internal morphologies were then observed at magnifications between 50x and 10000x.

2.4.4 Fiber analysis and pore size distribution

Fiber diameter and pore size distribution of beads were carried out to differentiate the internal structure of beads. SEM micrographs with similar scales were initially taken. The diameter of fibers and pore size distribution within the beads were carried out using ImageJ and Origin Pro software, respectively. For the estimation of fiber diameter and pore size of the beads, 100 and 50 measurements were taken, respectively.

2.4.5 Attenuated total reflection Fourier transform infrared spectroscopy (ATR-FTIR)

ATR-FTIR analysis was carried out to analyze the functional groups of PVA-ALG beads before and after the chemical crosslinking process. The spectrometer (PerkinElmer®, UK) operated with a spectral resolution of 4 cm^{-1} within a range of 400 - 4000 cm^{-1}. Before the measurements, the beads were dried, crushed with a mortar, placed on a plate, and pressed with the same pressure between a prism where infrared light was internally

reflected at the crystal-bead interface to provide the intended information [33]. A precise peak allocation was carried by using SpectraGryph, spectroscopy software.

2.5 Characterization of wet beads

2.5.1 Swelling of PVA-ALG beads

Swelling tests were conducted to evaluate the gain in mass and volumetric expansion of PVA-ALG beads after immersion in water [31, 34]. The volume and mass of these beads were initially measured right after taking them out from the secondary crosslinking solution. The increment due to water uptake was followed for twenty-four hours, considering the quick water uptake of PVA-ALG beads reported in the literature [35]. Swelling analysis was performed on two separate batches of the different bead types. The average was calculated from ten individual measurements for every time point reported. The volume and mass swelling were calculated using Equ. (3), (4), and (5) [31, 36].

$$Volume\ Swelling\ (\%) = \frac{V_t}{V_0} - 1 * 100 \quad (3)$$

$$Mass\ swelling\ (\%) = \frac{m_{f-}m_0}{m_0} * 100 \quad (4)$$

$$Volume = \frac{4}{3}\pi r^3 \quad (5)$$

Where r represents the radius of beads, $V_{0,}$ and $V_{t,}$ the volume of dry and wet beads in cm^3, and m_f and m_o represent the beads' final wet and dry mass in grams, respectively.

2.5.2 Hardness of PVA-ALG beads

Compression tests were carried with slight modifications of the protocol described by Kim et al. [37] to determine the effect of bead formulations on PVA-ALG bead hardness. PVA-ALG beads were compressed using a texture analyzer (TA-XT plus, Stable Micro Systems, UK) attached with a 5 kg force transducer and a cylindrical probe with a 15 mm diameter, as schematically shown in Fig. 2. A probe with a flat end was used to compress the beads 1.5 mm distance and return to its original height. A fast compression speed (0.5 mm. $s^{-1)}$ was set to reduce any time-dependent behaviors due to water loss. Ten measurements were taken for each bead type, and the maximum load the beads withstood was averaged. All maximum peak calculations were performed using Texture Exponent 5.0 software (Stable Micro Systems, UK).

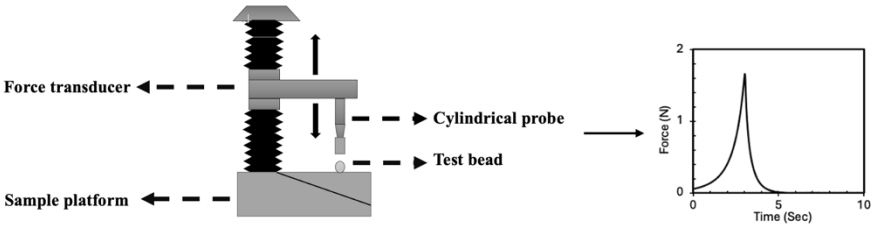

Fig. 2 Schematic illustration of compression tests of PVA-ALG bead

2.6 Mass transfer experiment: AHL incorporation

C6-, C8-, and C10-HSL incorporation onto vacant PVA-ALG beads were carried by batch experiments. Short and medium acyl chain length AHLs were specifically selected considering their abundance in MBRs and for the analysis of the effect of acyl chain length on their incorporation into beads [38, 39]. First, C6-, C8-, and C10- HSL, initially dissolved in acetonitrile, were adjusted to a concentration of 0.1 g. L^{-1}. Then, the required amount of AHL mixture solution was withdrawn from this stoke and added to beakers containing 200 mL tap water to have a final AHL mixture concentration of 200 µg. L^{-1}. After, the different types of beads were introduced to their respective beakers. The volumetric proportion of the beads with respect to the working

solution was 9% v/v. A control beaker containing only AHLs was also set to check if the decrease in AHL concentration is attributed only to their incorporation but not to natural degradation or precipitation. All the solutions were continuously stirred at 500 rpm. Afterward, a 200 µL sample was collected from each beaker for the first five hours. Immediately after collecting the samples, a two-microliter of 12 M HCl solution was added to adjust pH and preserve AHLs from degradation [40]. The AHL samples were dried in a speed vacuum (Eppendorf concentrator 5301, Germany) at 30^0C to extract the AHLs. After drying, a 40% Acetonitrile and water solution was added to redissolve the AHLs, followed by stirring and sonication steps to facilitate the AHL dissolution. The AHL extract was analyzed using UHPLC-MS/MS (UHPLC-RS 3000 Dionex® and MS-QTRAP 4500 AB Sciex®, respectively), an advanced quadrupole mass spectrometer. The extract containing AHLs were then passed inside the AQUITY UPLC BEH C18 column (Particle size -1.7 µm, 2.1x 50 mm, Waters Corp., USA). The mobile phase comprised solvent A (H_2O + 0.1% HCOOH) and solvent B (CH_3CN + 0.1% HCOOH) [34]. A gradient elution with a flow rate of 0.3 $mL.min^{-1}$ was employed throughout the separation. ESM table S1 further provides information on parameters for gradient elution. For each bead type, the AHL incorporation analysis was duplicated.

3. Result and discussion

This section presents the comprehensive findings obtained from the characterization of PVA-ALG beads. A detailed comparative evaluation of results from various characterization techniques, including different drying methods, SEM, N_2 physisorption, ATR-FTIR, and UHPLC-MS/MS analysis, are discussed.

3.1 Effect of change in PVA/SA mixture preparation on viscosity

The viscosity of PVA/SA mixtures is a critical parameter determining the physicochemical properties of PVA-ALG beads. It gives clear insight into the conformational arrangement of the polymer chains, which is integral to understanding the structural, swelling behavior, and mechanical properties of PVA-ALG beads in relation to the mixtures' concentration and dissolution method followed [25, 26, 41]. As summarized in Table 2, the viscosity of PVA/SA mixtures OPA10, US-10, and OPA8 was measured at 2.86 (± 0.5) Pa. s, 1.9 (± 0.4) Pa.s, and 1.2 (± 0.04) Pa. s, respectively. These results align with the findings by Mwiiri et al. [42], in which the viscosity of low (68 kDa) and high molecular weight (186 kDa) PVA with concentrations ranging from 5% to 20% wt. were reported between 0.09 to 40.2 Pa.s.

Table 2 Summary of the viscosity for PVA-ALG mixtures and control solutions solely composed of either PVA or SA

#	Polymer mixture	Polymer mixture concentration (% w/v)		Method of dissolution	Viscosity (Pa. s) ± SD	Surface tension ($mN.m^{-1}$) ± SD
		PVA	SA			
1	OP10	10	-	Oven	1.23 ± 0.17	-
2	US-P10	10	-	Ultrasonication	0.73 ± 0.06	-
3	OP8	8	-	Oven	0.17 ± 0.07	-
4	O-A1	-	1	Oven	0.030 ± 0.003	-
5	US-A1	-	1	Ultrasonication	0.02 ± 0.01	-
6	OPA10	10	1	Oven	2.86 ± 0.50	56.27 ± 0.55
7	US-10	10	1	Ultrasonication	1.90 ± 0.40	56.15 ± 0.33
8	OPA8	8	1	Oven	1.20 ± 0.04	55.66 ± 0.55

Upon comparing the viscosities of the polymer mixtures OPA10 and US-10, both prepared under the same PVA/SA concentration but different dissolution methods, it was recorded that the OPA10 polymer mixture, which is dissolved in a heating oven, exhibited 33% higher viscosity compared to US-10 mixture where ultrasonication is applied. Ultrasonic treatment is recognized for its ability to cause the scission of polymer main

chains, reducing molecular weight. Acoustic waves generated during sonication trigger microbubble formation, which collapses, causing cavitation [27, 43]. This cavitation effect is accompanied by a rise in temperature in the water bath, resulting in intense heating [25, 44]. Consequently, the –[CH_2CHOH]- and monosaccharide units of PVA and SA cleave, diminishing molecular weight, hence the viscosity of the mixture [25, 45]. Previous studies have reported analogous observations, wherein ultrasonic treatment led to decreased viscosity of both PVA and SA [43, 45]. A study by Rahamadiawan et al. [29] and Abral et al. [25] reported that ultrasonication of PVA mixtures also results in the disaggregation of the polymers and generates more individual polymer chains with free hydroxyl groups available for interaction during the chemical crosslinking process. Such effects of ultrasonication influence chain conformation and entanglement of both polymers inside the mixture [27]. The higher viscosity measured when the mixture was dissolved using a heating oven indicates the dissolution method does not induce significant chain scission, thereby preserving the chain entanglement [45]. This observation is further validated as the control solutions comprising either PVA or SA show a similar trend, as summarized in Table 2. When conducting a comparative analysis of control mixtures OP10 and US-P10, each containing 10% w/v PVA, the viscosity was measured to be 1.23 ± 0.17 and 0.73 ± 0.06 Pa. s, corresponding to a 40% difference.

Similarly, in the solutions US-A1 and O-A1, composed of only SA, the viscosities were 0.03 Pa. s and 0.02 Pa. s, respectively, corresponding to a 33% difference. The change in concentration of PVA to 8% w/v in the OPA8 mixture yields a viscosity of 1.2 ± 0.04 Pa. s, which agrees with the study reported by Rafiq et al. [46]. The reduction in viscosity is attributed to the presence of less solid PVA in the mixture for the same volume of water, resulting in fewer interactions between the polymer chains, making it easier for the polymer mixture to flow, hence reducing the viscosity. The surface tension of PVA/SA mixtures remains almost similar regardless of the changes in preparation conditions, as summarized in Table 2. This indicates the surface of the polymer mixture is saturated, and intermolecular interaction between PVA and SA is consistent throughout [42]. In general, viscosity analyses indicated a change in the concentration of PVA, and the methodology employed for mixture dissolution impacts the PVA/SA viscosity.

3.2 Selection of bead drying procedure

The textural properties, such as porosity, pore size, and specific surface area, play an integral role in the overall efficacy of QQ. High specific surface area and porosity offer an optimal environment for microbial attachment, colonization, and nutrient delivery [14]. For precise characterization of textural properties, along with the internal and external structures of the PVA-ALG beads, it is imperative to employ a drying methodology that preserves their texture and structure [32]. This section discusses the results of coupling N_2 physisorption and SEM analysis of evaporative, freeze, and supercritical CO_2 (SC-CO_2) dried OPA10 beads. This bead type was chosen for later application of the chosen drying technique across all the newly formulated beads.

According to previous studies by Robatzier et al. [32], Conzatti et al. [31], and Rodriguez et al. [47], evaporative, freeze, and SC-CO_2 drying procedures form dry polymer solids known as Xerogels, Ccryogels, and Aerogels, respectively [26, 27, 43]. Textural properties of a selected bead type after undergoing different drying procedures are also summarized in Table 3. The N_2 physisorption analysis revealed that the BET surface area of cryo- and aerogel beads was 0.83 m^2/g and 16.8 m^2/g, respectively. Information was not obtained on the BET surface area, porosity, or pore size of xerogels, which were recorded below the detection limit of the analysis equipment. SEM micrographs of evaporative heat-dried beads further elucidated compact bead structure with no visible external or internal porosity, as shown in Fig. 4 a to c. This is due to the evaporative drying procedure drawing tension at the meniscus of the solvent-vapor interface and leading to the complete collapse of the pores. The colloidal units are drawn to each other, forming beads with a "donut" like internal structure. These beads also undergo a shrinkage of around 56% from their wet size.

A relatively low specific surface area and narrow pore distributions were also recorded for the freeze-dried beads. This is due to the drying process inducing the formation of large macroporous cavities and very narrow pores due to the crystallization of water inside the beads. This is further elucidated in Fig. 4 d to f as the surface of freeze-dried beads possesses a non-spherical and uneven surface with wrinkles, which has been reported to be due to evaporation-induced surface tension [31]. The freeze-dried beads also undergo shrinkage of around 39%.

On the other hand, high specific surface and porosity were obtained for the SC-CO_2 dried beads due to the absence of surface tension in the pores during the SC-CO_2 drying procedure, which maintains pore structure [31, 32]. These results are consistent with the findings reported in the literature for polysaccharide-based films after SC-CO_2 drying [31]. The SEM micrographs in Fig. 4 g also confirm that SC-CO_2 dried beads demonstrate sphericity, a smooth external surface, and a porous internal structure. These improved structural appearances are attributed to the elimination of surface tension at the liquid-vapor interface, inhibiting denaturation and collapse of the surface and internal pore structure [31]. Fig. 3 presents the nitrogen physisorption isotherms, which provide information on the overall porosity and the cumulative pore size distribution of freeze and SC-CO_2 dried beads. A type IV adsorption-desorption isotherm characteristic for mesoporous materials dominated the porosity of beads in both drying procedures. The cumulative pore volume and pore sizes of SC-CO_2 dried beads were approximately 0.1 cm^3/g and 2 nm to 50 nm, respectively. The cumulative pore volume < 0.006 cm^3/g and narrow pore sizes ranging between 2 nm to 7 nm were recorded for the freeze-dried beads. The small pore size distribution in freeze-dried beads is attributed to the crystallization of water inside the bead structure, which causes the formation of very narrow pores in addition to excessively large cavities. The cumulative pore volume distribution of SC-CO_2 dried beads is much greater than freeze-dried beads, as SC-CO_2 beads relatively maintain the porous structure and internal polymer chain crosslinking density. Despite the favorable cumulative pore volume and size distributions of SC-CO_2 dried beads, it should be noted that the N_2 adsorption method can also underestimate the adequate pore size of the SC-CO_2 dried beads [31]. The analysis method can only detect pores with sizes below 100 nm, leading to undervaluation of macroporosity in the PVA-ALG beads, which has also been reported in the literature [31, 32]. The relatively high textural properties (pore size, volume, and surface area) of SC-CO_2 were found to be a more reliable drying technique for PVA-ALG beads than freeze and evaporative drying techniques. In addition to the textural properties, SEM analysis confirmed that SC-CO_2 preserves the porous structure of the bead's internal matrix, unlike the evaporative and freeze-dried beads, which display collapsed and cavitated pore structures. In conclusion, the texture and structural properties of SC-CO_2 dried beads are considered close to the hydrated state, enabling further analysis of the formulated beads using this drying technique.

Table 3 Overall data on BET surface area, pore size, and porosity of OPA10 beads for supercritical CO_2, freeze, and evaporative heat drying procedures.

Drying procedure	Temperature (^0C)	BET surface area (m^2/g)	Pore size (nm) (DFT)	Porosity	Shrinkage (%)
Supercritical CO_2	31.5	16.8	2-50	Mesoporous	42.5
Freeze drying	-50	0.83	2-7	Mesoporous	39
Evaporative heat	50	-	-	-	56

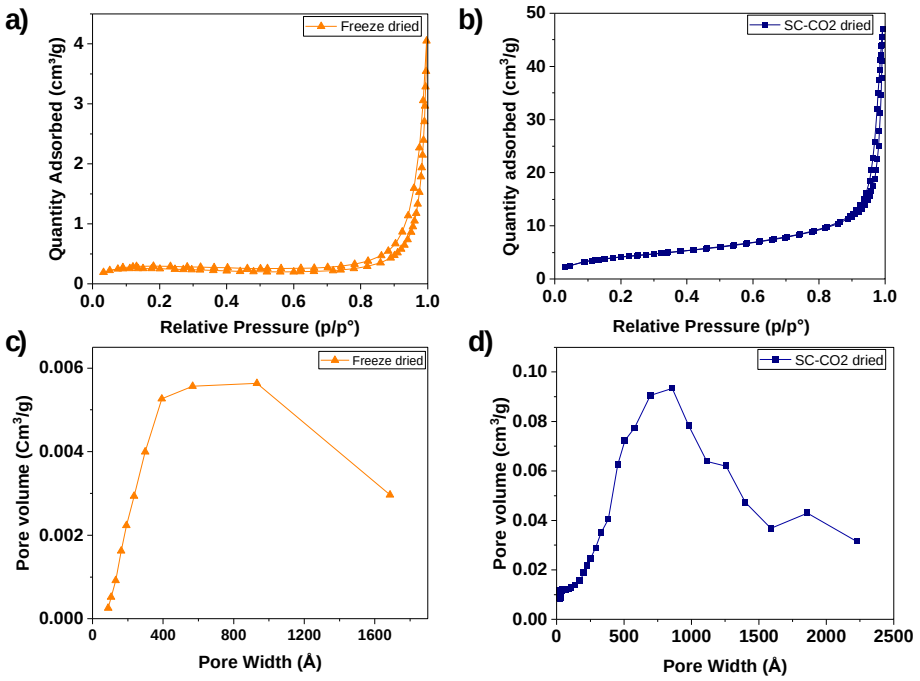

Fig. 3 a-b) N_2 physisorption isotherm and c-d) Cumulative pore size distribution of SC-CO_2 dried and freeze-dried beads

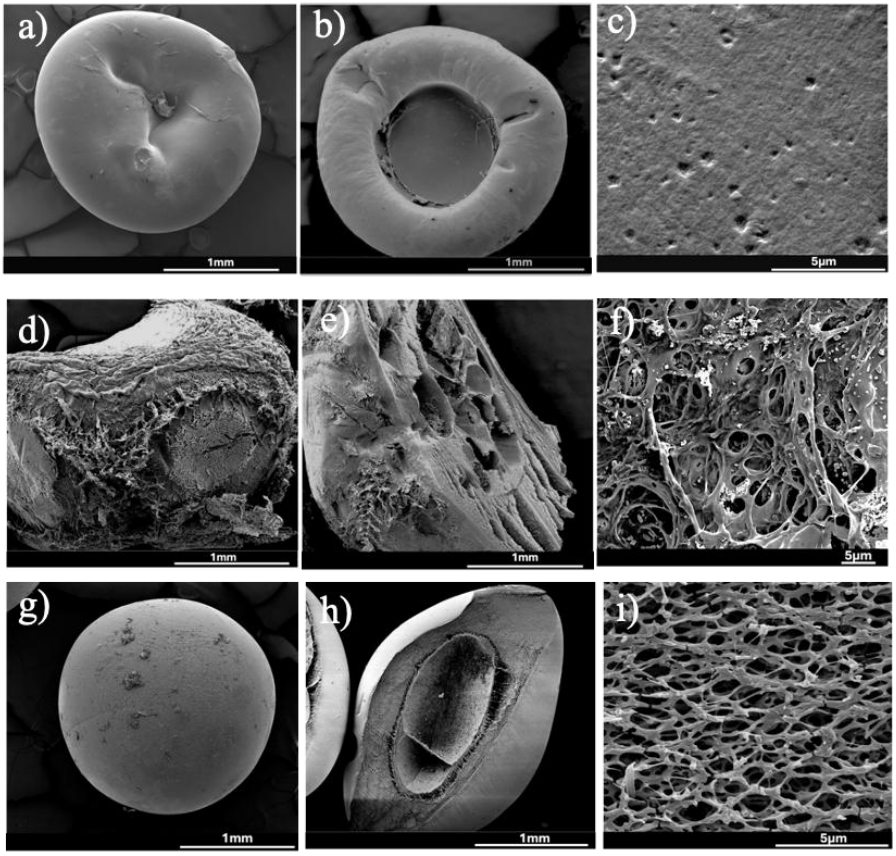

Fig. 4 SEM micrographs of surface, cross-sectional, and internal morphology of a to c) Evaporative, d to f) Freeze, and g to i) SC-CO_2 dried PVA-ALG beads with the surface (a, d, and g) and internal porous structure (b, c, e, f, h, and i) of selected OPA10 beads.

3.3 Physicochemical characterization of supercritical CO_2 dried PVA-ALG beads

After selecting supercritical CO_2 as a reliable drying technique, the formulated PVA-ALG beads underwent drying and characterization to comprehensively investigate the impacts of change in bead formulation on surface and internal morphology, as well as their specific surface area, pore size, and overall porosity.

3.3.1 Characterization of surface and internal structure of PVA-ALG beads

The SEM micrographs presented in Fig. 5 and Fig. 6 demonstrate surface and internal morphology of PVA-ALG beads, respectively. The surface of PVA-ALG beads appears to be smooth. The presence of low surface tension during the SC-CO_2 drying process helps minimize capillary forces, which cause shrinkage and deformation of the surface structure of PVA-ALG beads [47]. The mitigation of capillary forces also diminishes the occurrence of surface roughness. Despite the surface of these beads appearing completely smooth and spherical, they also appear dense. Sanz-Horta et al. [47] reported this appearance due to the fast diffusion of CO_2 from the beads' surface during the depressurization step of supercritical CO_2 drying. Meanwhile, Chan et al. [48] reported excessive gelation of SA by Ca^{2+} ions near the surface responsible for this appearance.

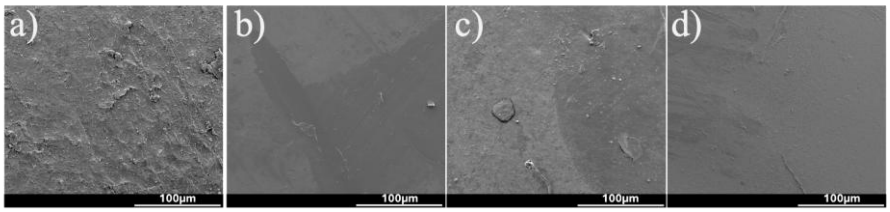

Fig. 5 Surface morphology of a) OPA10, b) US-10, c) OPA8, and d) SN-BA beads

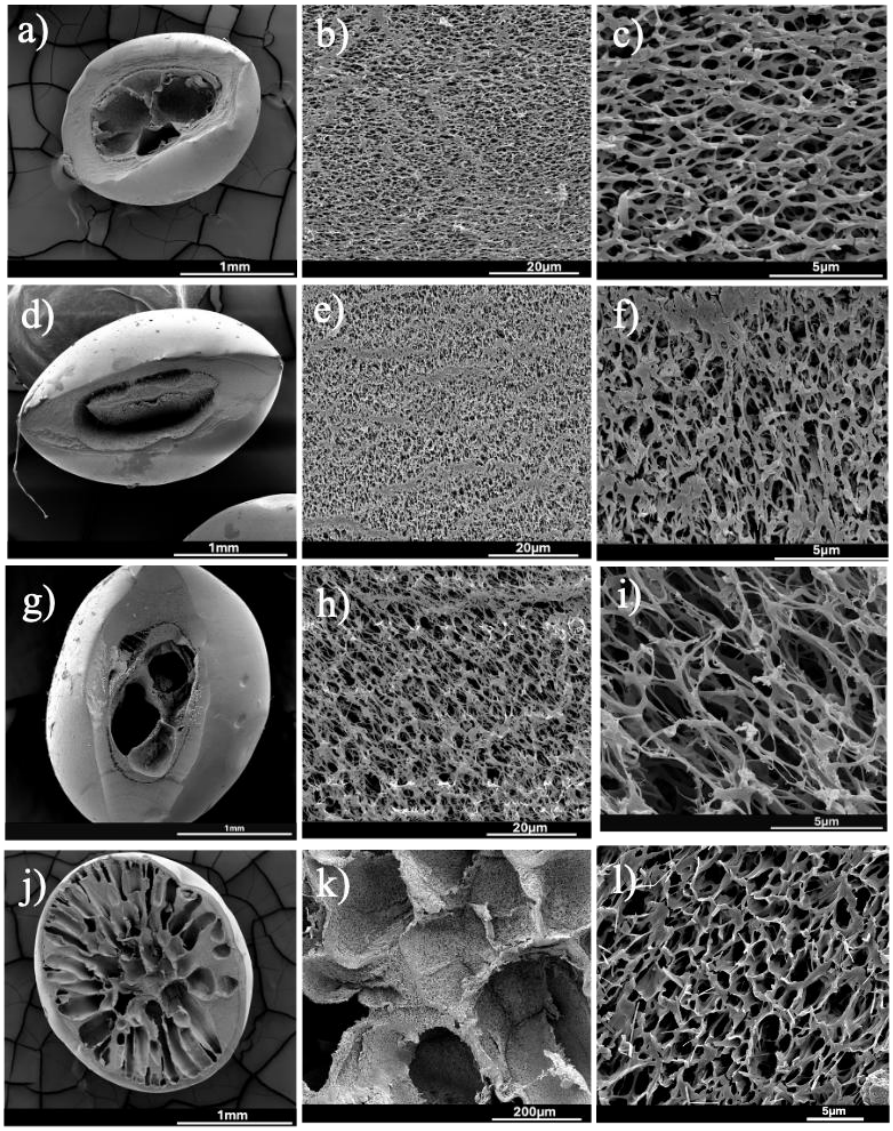

Fig. 6 SEM micrographs of the internal morphology of a to c) OPA10, d to f) US-10, g to j) OPA8, and j to l) SN-BA of supercritical CO_2 dried PVA-ALG beads

Fig. 6 a to l present SEM micrographs of the OPA10, US-10, and OPA8 beads. These beads were prepared using boric acid and calcium chloride as a primary crosslinking solution, followed by crosslinking in sodium sulfate solution. The possible chemistry of chemical crosslinking of PVA-ALG beads with $B[OH]_4^-$, SO_4^{2-}, and Ca^{2+} ions is also presented in ESM Fig.S1[20]. These beads are characterized by a highly interconnected pore network covered with thin skin layer. Upon crosslinking the PVA/SA mixtures by $B[OH]_4^-$ and Ca^{2+} ions, fast crosslinking occurs first at the periphery of beads, forming the skin layer [21]. Then, a portion of water is expelled from the solidified bead surface into the bead core, forming water-rich and lean layers. The skin layer further delays the diffusion of the crosslinking solution into the core, leading to slow crosslinking of PVA,

forming a densely interconnected chain network [21]. The delay in the crosslinking process can also be attributed to slow crosslinker diffusion in addition to chemical potential differences as the crosslinking process proceeds [49]. Similar findings regarding the appearance of interconnected pore networks in PVA-ALG beads have already been reported in the literature [21]. In addition, OPA10, US-10, and OPA8 exhibit hole-like structures in the cores of the beads. Candry et al. [21] suggested the presence of these hole-like structures to be due to the impact of the skin layer delaying diffusion of the crosslinking ions into the beads, resulting in the observed cavities.

The beads OPA10 shown in Fig. 6 c, composed of 10% w/v PVA and 1%w/v SA, exhibit porous internal structure characterized by significant polymer chain branching and well-defined chain orientation. Fig. 7 presents the fiber diameter and pore size distribution of OPA10 and US-10 beads. The mean pore size and fiber diameter in these beads were measured at 1.31 ± 0.4 µm and 0.24 ± 0.07 µm, respectively. Similarly, US-10 beads, produced with the same concentration of PVA but a different method of dissolution, demonstrate an internal structure with high chain crosslinking density with mean pore sizes and fiber diameters measured 0.83 ± 0.26 µm and 0.18 ± 0.05 µm, respectively. As explained in section 3.1, the dissolution of the PVA/SA mixture using ultrasonication results in chain scission and disaggregation of –[CH_2CHOH]n- and monosaccharide unit of PVA and SA, respectively. These short individual polymer chains crosslink, forming a structure with a significant crosslinking density. This is further elucidated as pore size distribution and fiber diameter of US-10 beads are relatively narrow compared to OPA10 beads, as presented in Fig. 7 c and d. Studies by Rahamadiawan et al. [50] and Zhang et al. [51] also reported similar observations where ultrasonication reduced the fiber diameter and sectioned the fibers of both cellulose and PVA films into shorter lengths. In addition, their study reported an increase in micro- and nanopores after ultrasonication. Meanwhile, OPA8 beads, composed of 8%w/v PVA, possess an internal structure featuring relatively larger pores and less chain branching, as shown in Fig. 6 g to i.

SN-BA beads were prepared using the blended primary crosslinking solution of boric acid, calcium chloride, and sodium nitrate, followed by crosslinking in sodium sulfate solution. Their internal pore structure consists of long protrusions resembling fingers, extending from the surface into the bead's core, as shown in Fig. 6 j. Beneath the finger-like structures, spongy-like pores can also be observed. These beads also don't exhibit cavities in their core like the OPA10, US-10, and OPA8. In addition to the polymer mixture concentration, one factor that dictates the pore morphology of polymer-based membranes and hydrogels is a difference in diffusion, hence, the crosslinking rate of the polymers with their respective ions [52]. Nielen et al. [52] reported the effect of different salts on polystyrene-alt-maleic acid (PSaMA) pore morphology. This study provided detailed information on how the rate at which the salt ions diffuse and interact with the polymer is dictated by diffusion rate and affinity, resulting in differences in the pore morphology of the membranes [52]. Macro-voids are also observed in membranes prepared using a bath blended with sodium nitrate and other salts (ionic strength > 0.3 M). In this regard, the presence of nitrate ions in the crosslinking solution has led to the modification of the crosslinking of PVA-ALG beads. The diffusion coefficients of ions involved in crosslinking the PVA-ALG beads are summarized in Table 4 [52–54]. Compared to $B[OH]_4^-$ ions, the diffusion coefficient of NO_3^- ions is much higher. Considering both these ions interact with PVA, this difference in diffusion may lead to uneven crosslinking as PVA has less time to organize and form uniformly crosslinked pore structures. As depicted in Fig. 6 l, spongy-like pores are also observed between and beneath the fingers. The occurrence of these pores could be due to the slow crosslinking of PVA by $B[OH]_4^-$ ions. In conclusion, SEM analysis of SC-CO_2 dried beads shows changes in the concentration of PVA, the method employed to dissolve the polymer concentration, and the composition of the crosslinking solution, which leads to the modification of pore morphology and chain entanglement.

Table 4 Diffusion coefficients of crosslinking ions used in our study [52–54]

Ion	Diffusion coefficient (D) (10^{-5} cm^2/s)
Ca^{2+}	0.79
Na^{+}	1.33
NO_3^{-}	1.90
H^{+}	9.31
Cl^{-}	2.03
$B[OH]_4^{-}$	0.51
SO_4^{2-}	1.07

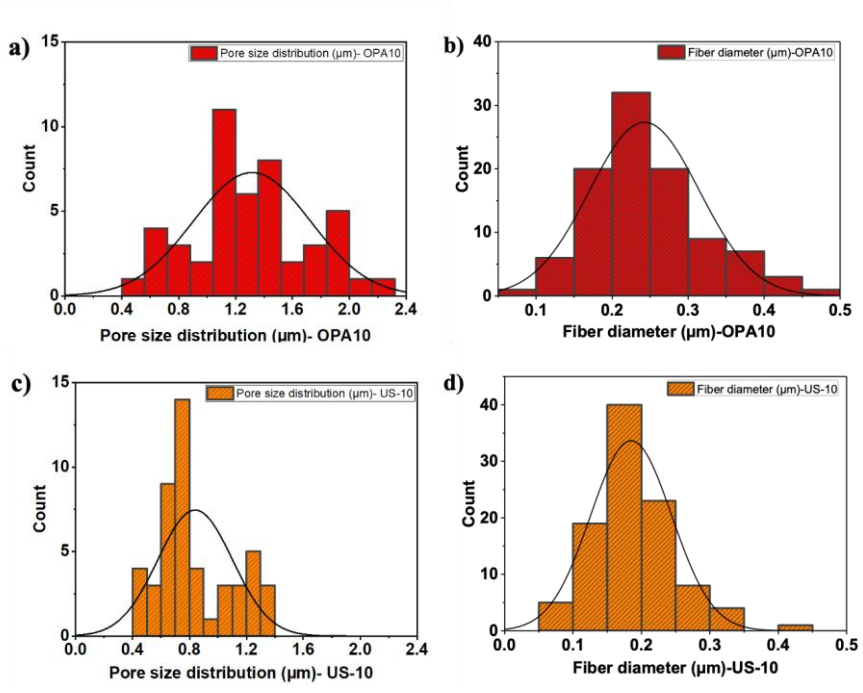

Fig. 7 Pore size and fiber diameter distribution of OPA10 beads (a and b) and US-10 beads (c and d)

3.3.2 Effect of change in preparation conditions on the textural properties

The impact of changes in PVA concentration, methods of dissolution, and crosslinking solutions composition on the textural properties of PVA-ALG beads are discussed in this section. Analysis results on porosity, BET surface area, and pore size distribution obtained from N_2 sorption analysis are all summarized in Table 5 and Fig. 8.

The N_2 adsorption-desorption isotherm of a selected SN-BA bead is shown in Fig. 8 a as representative for all formulated beads. The adsorption-desorption isotherm obtained appears to be an isotherm representing a type IV isotherm with an abrupt increase in nitrogen gas uptake at high relative pressure ranges and a saturation plateau characterized by an inflection point [32]. Adsorption occurs through the multilayer formation of N_2 molecules on the internal surface of the pores. The desorption branch of the isotherm shows an H1 hysteresis loop, which is observed in mesoporous materials with relatively narrow pore size distributions [32]. The BET surface area of OPA10, US-10, OPA8, and SN-BA beads reported in Fig. 8 b was measured ~17 m^2/g, 23 m^2/g, 16 m^2/g, and 17 m^2/g, respectively. These findings are consistent with the previous study reported by Du et al. [55], where the

BET surface area of PVA-ALG-$FeCl_3$ beads was reported to be around 19 m^2/g, with mesopores dominating the overall porosity [45]. The cumulative pore size distribution results obtained through the DFT and BJH models indicate that the PVA-ALG beads, OPA10, OPA8, US-10, and SN-BA, have pore sizes ranging between 4 and 40 nm and cumulative pore volume of 0.1 cm^3/g. ESM Fig. S2 further details cumulative pore size distributions of SC-CO_2 dried beads. Considering the pore sizes obtained, all formulated beads are mesoporous. The textural properties of SC-CO_2-dried PVA-ALG beads are similar among different bead types. BET surface area, pore size, and porosity are comparable despite different bead formulations. The observed resemblances can be attributed to the fact that, as indicated in Table 2, the surface tension (γ), a critical factor dictating the size of the bead droplet, is similar, leading to the creation of roughly the same size. Second is the notable shrinkage the beads undergo from a swollen state to aerogels after the SC-CO_2 drying. The shrinkage of the beads ranges between 41 % and 44 % of their original size, as reported in Table 5. Third is limitation of the analysis equipment, which is restricted to detecting pores below 100 nm. This prevents the detection of existing macropores within the beads.

The net molar energy (ΔE) and C-BET values are calculated to analyze the interaction strength between the first and consecutive adsorbate layers with nitrogen and bead surface. These results are summarized in Table 5. The ΔE was calculated between 2.57 $kJ.mol^{-1}$ and 2.66 $kJ.mol^{-1}$. Meanwhile, the C-BET values were 56 and 64, respectively. The highly crosslinked polymer network of OPA10, US-10, and OPA8 beads, which has been reported in Fig. 6 a to i, exhibit a much stronger affinity to the beads' surface due to the confinement of nitrogen gas in the pores, which enhances the interaction between nitrogen molecules and the bead's surface leading to relatively high ΔE and C-BET values [31]. The C-BET value (56) for SN-BA beads was relatively low, possibly due to the finger-like protrusions that don't confine the nitrogen gas much compared to other bead types. However, carefully considering the C-BET values must be made as mesopores artificially increase this value [31].

Bead type	Average Diameter wet beads (mm) ±SD	Shrinkage (%)	Pore size (nm) (DFT)	Pore Volume (cm^3/g) (BJH)	C-BET	Net molar energy (ΔE) ($kJ.mol^{-1}$)
OPA10	4.25 ± 0.03	42.5	4-40	0.1	64.3	2.66
US-10	4.40 ± 0.1	43.3	4.5-40	0.1	61.0	2.62
OPA8	4.23 ± 0.1	43.4	4-40	0.1	64.0	2.65
SN-BA	4.50 ± 0.01	40.7	4.5-20	0.1	56.0	2.57

Table 5 Textural properties of different PVA-ALG beads

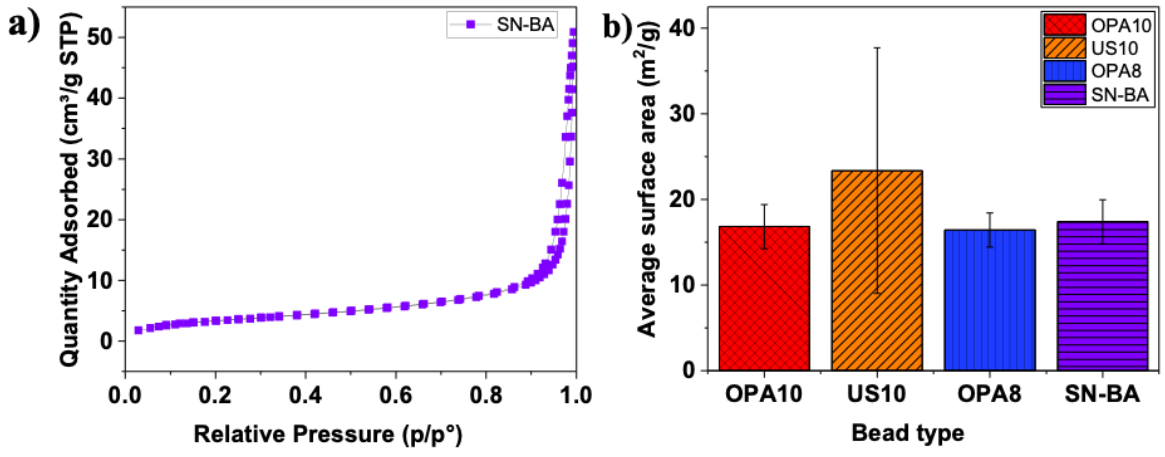

Fig. 8 a) N_2 adsorption-desorption isotherm of a selected SN-BA bead and b) BET surface area of all PVA-ALG beads

3.3.3 ATR-FTIR

ATR-FTIR analysis was conducted on PVA powder, SA powder, OPA10, US-10, OPA8, and SN-BA dried PVA-ALG beads to detect the alterations in functional groups pre- and post-chemical crosslinking process. ATR-FTIR spectra of pure PVA, SA powder, and chemically crosslinked beads prepared in different conditions are presented in Fig. 9. Peaks of interest have also been selected and marked. ESM Fig S3 also provides further information on the % Transmittance for all the peaks of interest.

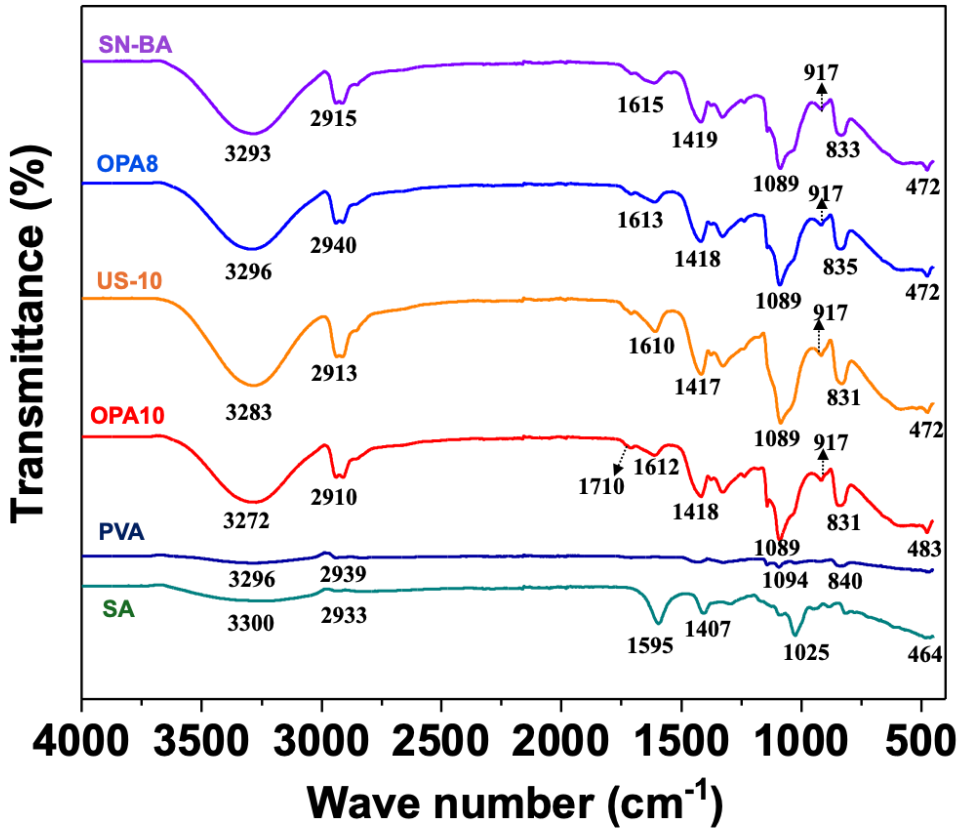

Fig. 9 ATR-FTIR spectra of pure PVA, Pure SA, and chemically crosslinked PVA-ALG beads

The primary peak of pure PVA exhibits broad, symmetric stretching vibrations of the -OH group around 3300 cm^{-1}. In addition, the -CH stretch, -CO stretch, and -C-C elongation of PVA were detected at 2939 cm^{-1}, 1094 cm^{-1}, and 840 cm^{-1}, respectively [33, 56]. A small band typical to asymmetric -C=O stretch from residual vinyl acetate precursor of PVA was observed at 1710 cm^{-1}. The -C=C- stretch attributed to acetyl groups of polyvinyl acetate, which is the precursor polymer of PVA reported by some studies, was not observed, which could be due to the high degree of hydrolysis PVA (> 99%) utilized in this study [33]. For SA, characteristic vibrations representing -OH stretch, -CH stretch, symmetric and asymmetric stretch of the -C=O bond of COO^- group of SA were recorded at 3300 cm^{-1}, 2933 cm^{-1}, 1595 cm^{-1}, and 1407 cm^{-1} [33, 57]. In addition, a characteristic peak

for SA representing O-Na^+ stretch is observed at 464 cm^{-1} [33]. Similar observations on the existing peaks of PVA and SA were also reported by Touzout et al.[58] and Pang et al.[59].

Following the chemical crosslinking of the PVA-ALG mixture, the peak intensity was observed for symmetric stretching of -OH groups, between 3296 cm^{-1} and 3272 cm^{-1} for all bead types. This increase is attributed to a high degree of crosslinking of hydroxyl -OH groups with $[B(OH)_4]^-$ and subsequently with SO_4^{2-} ions. Symmetric and asymmetric stretching vibrations of the -CO bond of COO^- group of SA, -CO, and -C-C stretching vibrations were detected at 1610 cm^{-1}, 1418 cm^{-1}, 1089 cm^{-1}, and 830 cm^{-1}, as summarized in **Erreur ! Source du renvoi introuvable.** [33, 57]. Spectral shifts observed from 1595 cm^{-1} to 1610 cm^{-1} and 1407 cm^{-1} to 1417 cm^{-1} of SA and crosslinked PVA-ALG beads is due to the replacement of Na^+ in guluronic acid residue by Ca^{2+} and, hence, a change in charge density and the radius of the atomic weight of the metal cation [57]. The shift observed from 1094 cm^{-1} to 1089 cm^{-1}, accompanied by spectral amplification, signifying the modifications occurring in the crystalline domains of PVA [33]. The beads OPA10, US-10, and SN-BA, composed of 10% PVA, the -OH stretches were observed at a relatively low wave number compared to OPA8 beads with 8% PVA. The -OH stretch observed at 3296 cm^{-1} for OPA8 beads is due to weaker hydrogen bonding, causing a spectral shift to a relatively higher wave number [60]. The vibration corresponding to the -CH stretch is also observed between 2910 cm^{-1} and 2940 cm^{-1}. For the beads OPA10 and US-10, the -CH stretch is observed at 2913 cm^{-1} and 2910 cm^{-1}. For the beads OPA8, the -CH stretch is marked at 2940 cm^{-1}. The spectral shift to a relatively higher wavenumber is again due to the low concentration of PVA, as few absorbing species are present compared to the beads composed of 10% w/v PVA concentration [27, 47]. The spectral shifts observed from 464 cm^{-1} to 472 cm^{-1} and 483 cm^{-1} in pure SA versus crosslinked beads are due to the replacement of Na^+ in the guluronic acid residue of SA by Ca^{2+}, leading to the formation of "Egg-box structure". Change in charge density and atomic radius of the cation leads to this spectral shift [57]. ATR-FTIR analysis confirmed that the chemical crosslinking of the PVA-ALG mixture resulted in spectral shifts compared to pure PVA and SA, further justifying the alterations in the chemical structure after cross-linking.

In conclusion, SEM analysis, ATR-FTIR, and N_2 physisorption technique effectively characterized the structural and textural properties of PVA-ALG beads dried using SC-CO_2. SEM analysis revealed significant changes in beads' internal pore structure, polymer chain branching, and pore sizes depending on different bead preparations followed. ATR-FTIR verified that the crosslinking of PVA-ALG alters the intensity and position of infrared peaks compared to pure PVA and SA, indicating structural chemical modifications post-crosslinking. All the formulated beads showed specific surface areas between 16 m^2/g and 24 m^2/g and pore sizes between 4 and 40 nm. Minor variations in BET surface area and pore size were recorded across different bead preparations, attributed to bead shrinkage post-SC-CO_2 drying and instrumental limitations restricting the detection of pore sizes above 100 nm.

3.4 Swelling properties of PVA-ALG beads.

The swelling behavior of PVA-ALG beads was analyzed, considering its contribution to structural and mechanical stability and adsorption properties [61, 62]. The swelling of PVA-ALG beads occurs due to their polymer chains absorbing water and the diffusion of water into the pores of the bead matrix [34, 36]. This property is primarily governed by crosslinking inside the bead's internal structure, which is influenced by type of crosslinking solution, polymer concentration, crosslinking time, and crosslinking rate between the polymers and crosslinkers [62]. The beads were immersed in water to assess the changes in both mass and volume, and the increments were followed for the first twenty-four hours. These findings are reported in Fig. 10. Kinetic analysis of mass swelling shows a significant contribution towards their equilibrium size in the first four hours, as depicted in ESM Fig. S4. The %volume swelling OPA10, US-10, OPA8, and SN-BA beads were also measured at 129%, 175%, 142%, and 129%, respectively, consistent with the findings of Lan et al. [34, 63]. Their study reported volume swelling of SA and powdered activated carbon/SA core-shell beads to be 116% and 177% [34]. Notably, % volume and mass swelling of US-10 beads are relatively high. This could be due to free hydroxyl groups even after crosslinking, which could enhance water uptake [23, 25, 39, 42]. Previous works reported that ultrasonication enhance moisture absorption in PVA films due to the exposure of the hydroxyl groups to the surface [29, 43, 64]. In comparison, beads OPA10, prepared in conditions similar to

those of US-10 except for a change in the dissolution method, exhibited 46% lower expansion in volume. OPA8 beads, with 8% w/v PVA, show relatively high-volume swelling compared to OPA10 beads due to existing porosity and fewer chain branching facilitating chain mobility, hence water uptake. SN BA beads also display a lower %volume swelling than US-10 and OPA8 beads.

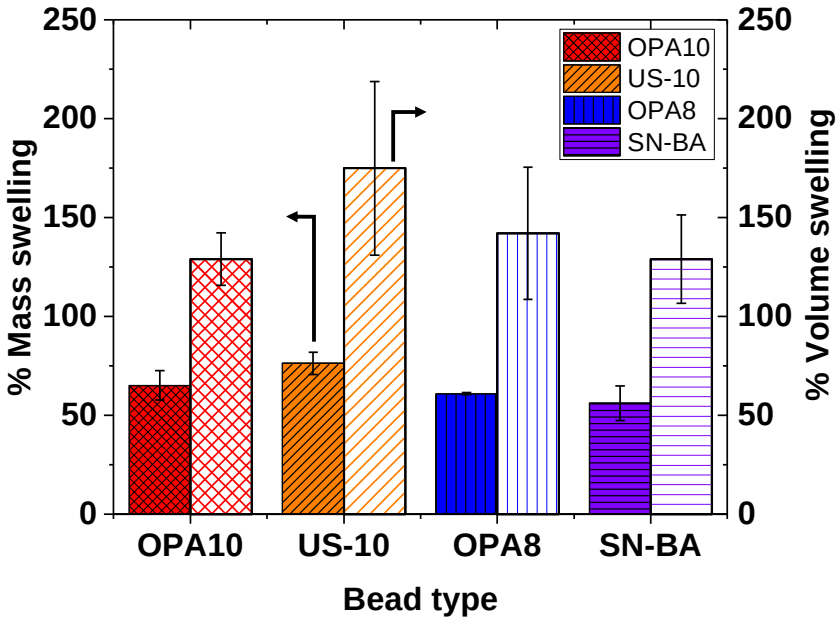

Fig. 10 Mass and volume swelling (%) of PVA-ALG beads

3.5 Hardness of PVA-ALG beads

Hardness related to the strength of beads is investigated considering the PVA-ALG bead physical washing effect in MBRs [37]. Variable hydrodynamic conditions persisting in MBRs create turbulence and different circulation frequencies, determining the collision recurrence of the beads with the filtration membrane [3]. Such changes in operation affect their mechanical stability [3, 36]. Fig. 11 presents the hardness of PVA-ALG beads, evaluated to analyze the bead resistance to deformation under constant compressive load. Based on the test results obtained, the hardness of OPA10, US-10, OPA8, and SN-BA beads was measured at 0.29 (± 0.05) N, 0.24 (± 0.03) N, 0.23 (± 0.01) N, and 0.15 (± 0.01) N, respectively. The beads OPA10 possess relatively high hardness compared to other bead types. This is due to extensive polymer chain branching and interconnection in the beads structure, which provides good mechanical stability [36]. In addition, as shown in Fig. 6 c, the polymer chains of these beads possess uniformity in arrangement, which generally leads to a more homogeneous distribution of the applied load when subjected to compression. For the beads US-10, hardness is 17% lower than OPA10 beads. Despite having a more densely interconnected chain structure, which should lead to better hardness, the limitation could have risen from the short PVA chains shown in Fig. 6 e, which possess short ends, making them respond to the applied load relatively easily. In addition, the swelling of US-10 beads is also higher. When the beads swell, they become soft and less rigid [61]. The polymer chains move more freely, reducing crosslinking effectiveness and potentially affecting the hardness of US-10 beads [27]. OPA8 beads also exhibit lower hardness due to their more porous internal structure and enhanced water uptake. In contrast, SN-BA beads exhibit the least hardness than the other beads. This is attributed to the finger-like pores, which create weak spots for the bead structure to collapse [49]. The relatively weaker hardness of SN-BA beads might have some implications for their long-term performance in MBRs. These results highlight the differences in the bead's internal structure resulting from variations in polymer mixture concentration. Additionally, the composition of the crosslinking solution also plays a substantial role in dictating their hardness.

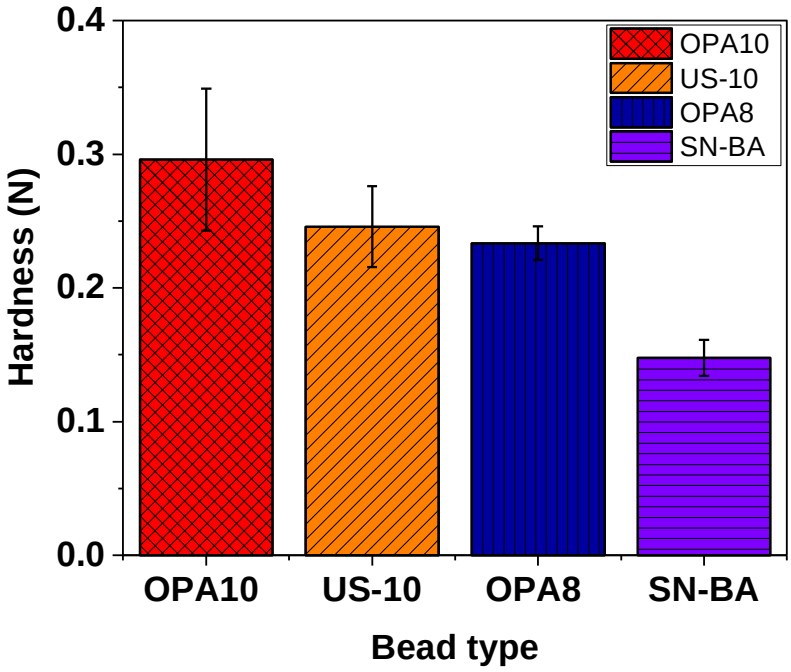

Fig. 11 Hardness (in Newtons) of PVA-ALG beads prepared in different conditions

3.6 Incorporation of AHLs

The incorporation of AHL molecules with short and medium chain lengths onto PVA-ALG was examined to evaluate the adsorption capacity of the newly prepared beads. The results representing the incorporation kinetics of AHLs onto SN-BA beads and the incorporated C6-, C8-, and C10-HSL quantity (%) for all bead types are presented in Fig. 12. The incorporation kinetics for selected SN-BA beads, reported as a representative for all beads, shows AHL incorporation occurs in the first hour. A similar tendency was observed in almost all remaining bead types. AHL incorporation follows a trend where the incorporation of AHLs with shorter acyl chain lengths (C6-HSL) is comparably higher than those possessing medium chain lengths (C8-HSL and C10-HSL). AHLs with short acyl chains are less hydrophobic than long-chain AHLs, allowing the hydrophilic PVA-ALG beads to have a relative affinity, hence higher incorporation on the beads [65]. SN-BA beads possess a higher AHL incorporation capacity than other bead types. SN-BA beads adsorbed around 30%, 24%, and 23% of the initial C6-, C8-, and C10-HSL concentration, respectively. The finger-like pore structures enhance AHL permeation by shortening the transport pathway to the spongy pores in the beads [49]. Kim et al. [4], who reported the first QQ-beads composed of SA, explained spacious pore structures within the beads provide a good environment for bacterial colonization and offer low mass transfer resistance, allowing easy permeation of AHL molecules, which led to a very effective degradation of C8-HSL by the QQ-bacteria. AHL incorporation measured for OPA10, US-10, and OPA8 beads possessing interconnected pores are also summarized in Fig. 12 b. The amount of C6-, C8-, and C10-HSL onto these bead types is notably lower. This is attributed to the densely crosslinked pores that can hinder the permeation of AHLs into the beads compared to the finger-like pores [49]. US-10 and OPA10 beads, composed of 10% PVA, possess high AHL incorporation compared to OPA8 beads with 8% w/v PVA. The internal structure with highly interconnected chains provides more surface for the AHLs to adhere to, enhancing incorporation. Recently, Kim et al. [66] reported the incorporation of C8-HSL onto vacant PVA/SA beads around 15%, close to the quantity incorporated on vacant OPA10, US-10, and OPA8 beads in our study. These findings indicated that the beads' internal structure significantly affects AHL incorporation. The finger-like pore structure induces significant AHL permeation to the spongy-like pores beneath, hence high incorporation capacity.

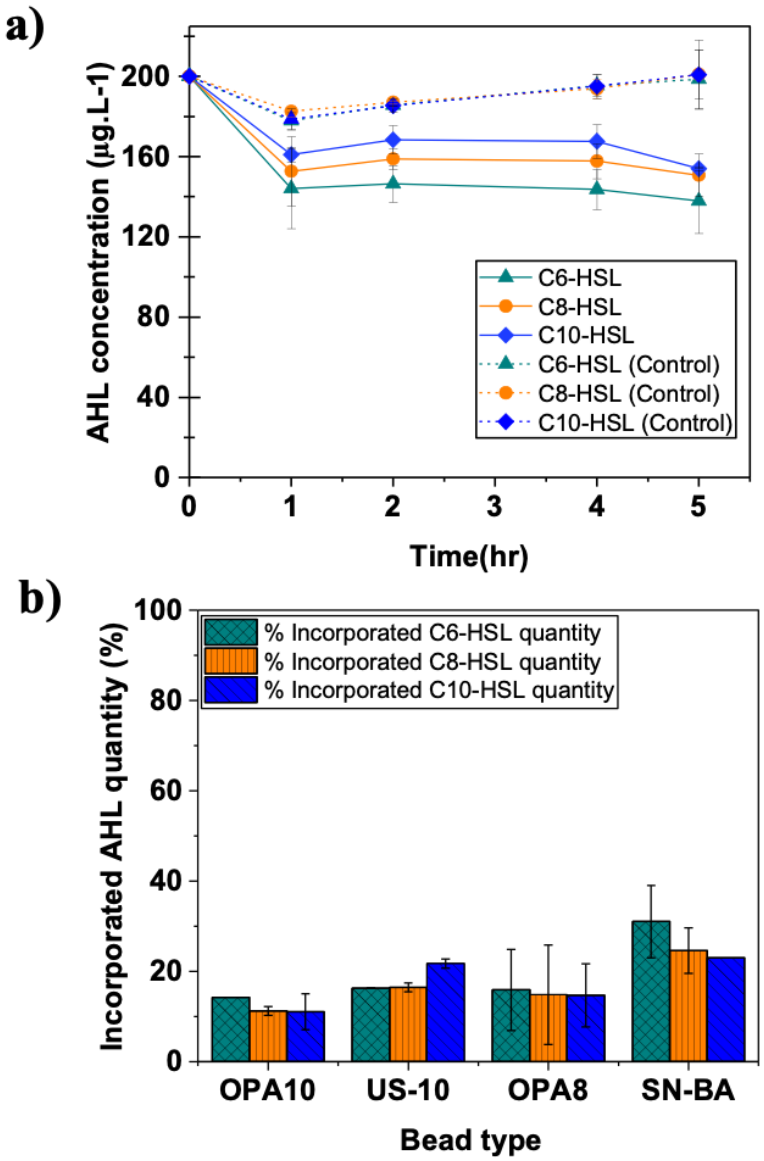

Fig. 12 a) The incorporation kinetics of AHLs for SN-BA beads and b) Incorporated C6-, C8-, and C10-HSL quantity (%) on all formulated bead types

4. Conclusion

This study present novel approaches for preparing and characterizing PVA-ALG beads for QQ applications. Specifically, findings on the impacts of change in PVA concentration, the methodology employed to dissolve the PVA/SA mixture, and the composition of the crosslinking solution on the structural, textural, mechanical, swelling properties, and AHLs incorporation capacity of different beads were discussed. In conclusion,

1) Changes in PVA concentration and the technique employed to dissolve the PVA/SA mixture influence viscosity, giving clear insight into the effects of the polymer mixture's composition on PVA-ALG beads' physicochemical properties.

2) Comparison between evaporative heat drying, freeze, and SC-CO_2 drying techniques revealed that SC-CO_2 drying maintains beads' internal and external porous structure, compared to freeze- and evaporative drying, which induced significant bead structure modifications.

3) PVA-ALG beads crosslinked using boric acid and calcium chloride crosslinking solution provide internal structure with significant polymer chain crosslinking density. Meanwhile, beads prepared by blending the primary crosslinking solution of boric acid and calcium chloride with sodium nitrate result in beads with internal structures with long finger-like protrusions.

4) PVA-ALG beads are mesoporous, with specific surface areas ranging from 16 m^2/g to 23 m^2/g. Swelling analysis revealed that the beads possess different degrees of swelling due to differences in porosity and hydrophilic nature.

5) Beads with internal structures possessing high chain crosslinking density demonstrate superior hardness compared to beads with finger-like pores.

6) Beads with finger-like pore structures exhibited excellent AHL incorporation capacity compared to beads with densely cross-linked chains. The finger-like pores enhance the permeation of AHLs into the beads. Also, AHL with shorter acyl chains (C6-HSL) were more incorporated readily than those with medium chain lengths (C8-HSL and C10-HSL).

Reference

Iqbal T, Lee K, Lee CH, Choo KH (2018) Effective quorum quenching bacteria dose for anti-fouling strategy in membrane bioreactors utilizing fixed-sheet media. J Memb Sci 562:18–25. https://doi.org/10.1016/j.memsci.2018.05.031

Iqbal T, Shah SSA, Lee K, Choo KH (2021) Porous shell quorum quenching balls for enhanced anti-biofouling efficacy and media durability in membrane bioreactors. Chemical Engineering Journal 406:. https://doi.org/10.1016/j.cej.2020.126869

Bouayed N, Dietrich N, Lafforgue C, et al (2016) Process-oriented review of bacterial quorum quenching for membrane biofouling mitigation in membrane bioreactors (MBRs). Membranes (Basel) 6:. https://doi.org/10.3390/membranes6040052

Kim SR, Oh HS, Jo SJ, et al (2013) Biofouling control with bead-entrapped quorum quenching bacteria in membrane bioreactors: Physical and biological effects. Environ Sci Technol 47:836–842. https://doi.org/10.1021/es303995s

Bouayed N, Montaner M, Le Men C, et al (2022) Experimental Solid–Liquid Mass Transfer around Free-Moving Particles in an Air-Lift Membrane Bioreactor with Optical Techniques. Fluids 7:. https://doi.org/10.3390/fluids7100338

Acet Ö, Erdönmez D, Acet BÖ, Odabaşı M (2021) N-acyl homoserine lactone molecules assisted quorum sensing: effects consequences and monitoring of bacteria talking in real life. Arch Microbiol 203:3739–3749 https://doi.org/10.1007/s00203-021-02381-9

Muras A, Parga A, Mayer C, Otero A (2021) Use of Quorum Sensing Inhibition Strategies to Control Microfouling. Mar Drugs 19:. https://doi.org/10.3390/md19020074

Köse-Mutlu B, Ergön-Can T, Koyuncu I, Lee CH (2019) Quorum quenching for effective control of biofouling in membrane bioreactor: A comprehensive review of approaches, applications, and challenges. Environmental Engineering Research 24:543–558. https://doi.org/10.4491/eer.2018.380

Lee K, Lee CH, Choo KH (2021) A facile HPLC-UV-based method for determining the concentration of the bacterial universal signal autoinducer-2 in environmental samples. Applied Sciences (Switzerland) 11:2–9. https://doi.org/10.3390/app11199116

Cheong WS, Kim SR, Oh HS, et al (2014) Design of quorum quenching microbial vessel to enhance cell viability for biofouling control in membrane bioreactor. J Microbiol Biotechnol 24:97–105. https://doi.org/10.4014/jmb.1311.11008

Kim J, Bae E, Park H, et al (2024) Membrane reciprocation and quorum quenching: An innovative combination for fouling control and energy saving in membrane bioreactors. Water Res 250:. https://doi.org/10.1016/j.watres.2023.121035

Christiaen SEA, Brackman G, Nelis HJ, Coenye T (2011) Isolation and identification of quorum quenching bacteria from environmental samples. J Microbiol Methods 87:213–219. https://doi.org/10.1016/j.mimet.2011.08.002

Nahm CH, Kim K, Min S, et al (2019) Quorum sensing: an emerging link between temperature and membrane biofouling in membrane bioreactors. Biofouling 35:443–453. https://doi.org/10.1080/08927014.2019.1611789

Nabi M, Liang H, Zhou Q, et al (2023) In-situ membrane fouling control and performance improvement by adding materials in anaerobic membrane bioreactor: A review. Science of the Total Environment 865 http://dx.doi.org/10.1016/j.scitotenv.2022.161262

Islam ZU, Rose J, Ahmed S, Chung S (2020) Quorum Quenching Cell Entrapping Bead by Polyvinyl Alcohol Method for Biofouling Mitigation in Lab-scale MBR. NUST Journal of Engineering Sciences, 13:28–36. https://doi.org/https://doi.org/10.24949/njes.v13i1.601

Lee S, Lee SH, Lee K, et al (2016) Effect of the shape and size of quorum-quenching media on biofouling control in membrane bioreactors for wastewater treatment. J Microbiol Biotechnol 26:1746–1754. https://doi.org/10.4014/jmb.1605.05021

Islam ZU, Ayub M, Chung S, Oh H (2022) Effect of Aeration Intensity on Performance of Lab-Scale Quorum-Quenching Membrane Bioreactor. Membranes (Basel) 12:. https://doi.org/10.3390/membranes12030289

Lee S, Park SK, Kwon H, et al (2016) Crossing the Border between Laboratory and Field: Bacterial Quorum Quenching for Anti-Biofouling Strategy in an MBR. Environ Sci Technol 50:1788–1795. https://doi.org/10.1021/acs.est.5b04795

Wu KA, Wisecarver KD (1992) Cell immobilization using PVA crosslinked with boric acid. Biotechnol Bioeng 39:447–449. https://doi.org/10.1002/bit.260390411

Zain NAM, Suhaimi MS, Idris A (2011) Development and modification of PVA-alginate as a suitable immobilization matrix. Process Biochemistry 46:2122–2129. https://doi.org/10.1016/j.procbio.2011.08.010

Candry P, Godfrey BJ, Wang Z, et al (2022) Tailoring polyvinyl alcohol-sodium alginate (PVA-SA) hydrogel beads by controlling crosslinking pH and time. Sci Rep 12:20822. https://doi.org/10.1038/s41598-022-25111-7

Tsai CJ, Chang YR, Lee DJ (2018) Shape Stable Poly(vinyl alcohol) and Alginate Cross-Linked Hydrogel under Drying-Rewetting Cycles: Boron Substitution. Ind Eng Chem Res 57:14213–14222. https://doi.org/10.1021/acs.iecr.8b03420

Bouayed N, Cavalier A, Lafforgue C, et al (2020) Hydrodynamics Characterization of the Impact of Free-Moving Particles in an Air-Lift Membrane Bioreactor. Ind Eng Chem Res 59:7943–7954. https://doi.org/10.1021/acs.iecr.9b06749

Takei T, Ikeda K, Ijima H, et al (2012) A comparison of sodium sulfate, sodium phosphate, and boric acid for preparation of immobilized Pseudomonas putida F1 in poly(vinyl alcohol) beads. Polymer Bulletin 69:363–373. https://doi.org/10.1007/s00289-012-0756-4

Abral H, Atmajaya A, Mahardika M, et al (2020) Effect of ultrasonication duration of polyvinyl alcohol (PVA) gel on characterizations of PVA film. Journal of Materials Research and Technology 9:2477–2486. https://doi.org/10.1016/j.jmrt.2019.12.078

Mohod A V., Gogate PR (2011) Ultrasonic degradation of polymers: Effect of operating parameters and intensification using additives for carboxymethyl cellulose (CMC) and polyvinyl alcohol (PVA). Ultrason Sonochem 18:727–734. https://doi.org/10.1016/j.ultsonch.2010.11.002

Safronova EY, Yurova PA, Ashrafi AM, et al (2021) The effect of ultrasonication of polymer solutions on the performance of hybrid perfluorinated sulfonic acid membranes with SiO2 nanoparticles. React Funct Polym 165:. https://doi.org/10.1016/j.reactfunctpolym.2021.104959

Chen J, Chen Y, Li H, et al (2010) Physical and chemical effects of ultrasound vibration on polymer melt in extrusion. Ultrason Sonochem 17:66–71. https://doi.org/10.1016/j.ultsonch.2009.05.005

Rahmadiawan D, Abral H, Railis RM, et al (2022) The Enhanced Moisture Absorption and Tensile Strength of PVA/Uncaria gambir Extract by Boric Acid as a Highly Moisture-Resistant, Anti-UV, and Strong Film for Food Packaging Applications. Journal of Composites Science 6:. https://doi.org/10.3390/jcs6110337

Ding J, Zhang R, Ahmed S, et al (2019) Effect of sonication duration in the performance of polyvinyl alcohol/chitosan bilayer films and their effect on strawberry preservation. Molecules 24:. https://doi.org/10.3390/molecules24071408

Conzatti G, Faucon D, Castel M, et al (2017) Alginate/chitosan polyelectrolyte complexes: A comparative study of the influence of the drying step on physicochemical properties. Carbohydr Polym 172:142–151. https://doi.org/10.1016/j.carbpol.2017.05.023

Robitzer M, Tourrette A, Horga R, et al (2011) Nitrogen sorption as a tool for the characterisation of polysaccharide aerogels. Carbohydr Polym 85:44–53. https://doi.org/10.1016/j.carbpol.2011.01.040

Sun L, Wang J, Liang J, Li G (1234) Boric Acid Cross-linked 3D Polyvinyl Alcohol Gel Beads by NaOH-Titration Method as a Suitable Biomass Immobilization Matrix. J Polym Environ 28:532–541. https://doi.org/10.1007/s10924-019-01610-z

Lan T, Huang J, Ouyang Y, et al (2021) QQ-PAC core-shell structured quorum quenching beads for potential membrane antifouling properties. Enzyme Microb Technol 148:. https://doi.org/10.1016/j.enzmictec.2021.109813

Vidovic S, Stojkovska J, Stevanovic M, et al (2022) Effects of poly(vinyl alcohol) blending with Ag/alginate solutions to form nanocomposite fibres for potential use as antibacterial wound dressings. R Soc Open Sci 9:. https://doi.org/10.1098/rsos.211517

Zeng Z, Tang B, Xiao R, et al (2018) Quorum quenching bacteria encapsulated in PAC-PVA beads for enhanced membrane antifouling properties. Enzyme Microb Technol 117:72–78. https://doi.org/10.1016/j.enzmictec.2018.06.006

Kim SR, Lee KB, Kim JE, et al (2015) Macroencapsulation of quorum quenching bacteria by polymeric membrane layer and its application to MBR for biofouling control. J Memb Sci 473:109–117. https://doi.org/10.1016/j.memsci.2014.09.009

Yeon KM, Cheong WS, Oh HS, et al (2009) Quorum sensing: A new biofouling control paradigm in a membrane bioreactor for advanced wastewater treatment. Environ Sci Technol 43:380–385. https://doi.org/10.1021/es8019275

Honda R, Phan PT, Tobino T, et al (2019) Diversity of N-acyl homoserine lactones in activated sludge detected by Fourier transform mass spectrometry. NPJ Clean Water 2:. https://doi.org/10.1038/s41545-019-0035-0

Wang J, Quan C, Wang X, et al (2011) Extraction, purification and identification of bacterial signal molecules based on N-acyl homoserine lactones. Microb Biotechnol 4:479–490. https://doi.org/10.1111/j.1751-7915.2010.00197.x

Chen J, Chen Y, Li H, et al (2010) Physical and chemical effects of ultrasound vibration on polymer melt in extrusion. Ultrason Sonochem 17:66–71. https://doi.org/10.1016/j.ultsonch.2009.05.005

Mwiiri FK, Daniels R molecules Influence of PVA Molecular Weight and Concentration on Electrospinnability of Birch Bark Extract-Loaded Nanofibrous Scaffolds Intended for Enhanced Wound Healing. https://doi.org/10.3390/molecules25204799

Abral H, Atmajaya A, Mahardika M, et al (2020) Effect of ultrasonication duration of polyvinyl alcohol (PVA) gel on characterizations of PVA film. Journal of Materials Research and Technology 9:2477–2486. https://doi.org/10.1016/j.jmrt.2019.12.078

Arefi-Oskoui S, Khataee A, Safarpour M, et al (2019) A review on the applications of ultrasonic technology in membrane bioreactors. Ultrason Sonochem 58:104633. https://doi.org/10.1016/j.ultsonch.2019.104633

Dodero A, Vicini S, Castellano M (2020) Depolymerization of sodium alginate in saline solutions via ultrasonic treatments: A rheological characterization. Food Hydrocoll 109:. https://doi.org/10.1016/j.foodhyd.2020.106128

Rafiq M, Hussain T, Abid S, et al (2018) Development of sodium alginate/PVA antibacterial nanofibers by the incorporation of essential oils. Mater Res Express 5:. https://doi.org/10.1088/2053-1591/aab0b4

Sanz-Horta R, Martinez-Campos E, García C, et al (2021) Breath figures makes porous the "so-called" skin layer obtained in polymer foams prepared by supercritical CO2 treatments. Journal of Supercritical Fluids 167:. https://doi.org/10.1016/j.supflu.2020.105051

Chan ES, Lim TK, Voo WP, et al (2011) Effect of formulation of alginate beads on their mechanical behavior and stiffness. Particuology 9:228–234. https://doi.org/10.1016/j.partic.2010.12.002

Hołda AK, Vankelecom IFJ (2015) Understanding and guiding the phase inversion process for synthesis of solvent resistant nanofiltration membranes. J Appl Polym Sci 132:. https://doi.org/10.1002/app.42130

Rahmadiawan D, Abral H, Kotodeli RA, et al (2023) A Novel Highly Conductive, Transparent, and Strong Pure-Cellulose Film from TEMPO-Oxidized Bacterial Cellulose by Increasing Sonication Power. Polymers (Basel) 15:. https://doi.org/10.3390/polym15030643

Zhang R, Wang Y, Ma D, et al (2019) Effects of ultrasonication duration and graphene oxide and nano-zinc oxide contents on the properties of polyvinyl alcohol nanocomposites. Ultrason Sonochem 59:. https://doi.org/10.1016/j.ultsonch.2019.104731

Nielen WM, Willott JD, Esguerra ZM, de Vos WM (2020) Ion specific effects on aqueous phase separation of responsive copolymers for sustainable membranes. J Colloid Interface Sci 576:186–194. https://doi.org/10.1016/j.jcis.2020.04.125

Park JK, Lee' KJ (1994) Diffusion Coefficients for Aqueous Boric Acid

Goli E, Hiemstra T, Van Riemsdijk WH, et al (2010) Diffusion of neutral and ionic species in charged membranes: Boric acid, arsenite, and water. Anal Chem 82:8438–8445. https://doi.org/10.1021/ac1009436

Du Z, Liu F, Xiao C, et al (2021) Fabrication of poly(vinyl alcohol)/sodium alginate hydrogel beads and its application in photo-Fenton degradation of tetracycline. J Mater Sci 56:913–926. https://doi.org/10.1007/s10853-020-05299-7

Mansur HS, Sadahira CM, Souza AN, Mansur AAP (2008) FTIR spectroscopy characterization of poly (vinyl alcohol) hydrogel with different hydrolysis degree and chemically crosslinked with glutaraldehyde. Materials Science and Engineering C 28:539–548. https://doi.org/10.1016/j.msec.2007.10.088

Voo WP, Lee BB, Idris A, et al (2015) Production of ultra-high concentration calcium alginate beads with prolonged dissolution profile. RSC Adv 5:36687–36695. https://doi.org/10.1039/c5ra03862f

Touzout Z, Abdellaoui N, Hadj-Hamou AS (2024) Conception of pH-sensitive calcium alginate/poly vinyl alcohol hydrogel beads for controlled oral curcumin delivery systems. Antibacterial and antioxidant properties. Int J Biol Macromol 263:130389. https://doi.org/10.1016/j.ijbiomac.2024.130389

Pang H, Huang J, Li X, et al (2023) Enhancing quorum quenching media with 3D robust electrospinning coating: A novel biofouling control strategy for membrane bioreactors. Water Res 234:. https://doi.org/10.1016/j.watres.2023.119830

Falqi FH, Bin-Dahman OA, Hussain M, Al-Harthi MA (2018) Preparation of miscible PVA/PEG blends and effect of graphene concentration on thermal, crystallization, morphological, and mechanical properties of PVA/PEG (10wt%) blend. Int J Polym Sci 2018:. https://doi.org/10.1155/2018/8527693

Fumio U, Hiroshi Y, Kumiko N, et al (1990) Swelling and mechanical properties of poly(vinyl alcohol) hydrogels. Int J Pharm 58:135–142. https://doi.org/10.1016/0378-5173(90)90251-X

Aljinat S (2019) Synthesis and Swelling Behavior of Sodium Alginate / Poly (vinyl alcohol) Hydrogels. 16:252–260. https://doi.org/10.4274/tjps.galenos.2018.92408

Lan T, Huang J, Ouyang Y, et al (2021) QQ-PAC core-shell structured quorum quenching beads for potential membrane antifouling properties. Enzyme Microb Technol 148:. https://doi.org/10.1016/j.enzmictec.2021.109813

Abral H, Lawrensius V, Handayani D, Sugiarti E (2018) Preparation of nano-sized particles from bacterial cellulose using ultrasonication and their characterization. Carbohydr Polym 191:161–167. https://doi.org/10.1016/j.carbpol.2018.03.026

Coquant G, Grill JP, Seksik P (2020) Impact of N-Acyl-Homoserine Lactones, Quorum Sensing Molecules, on Gut Immunity. Front Immunol 11 doi: 10.3389/fimmu.2020.01827

Kim H, Noori A, Kim MH, et al (2024) Biofouling mitigation of a membrane bioreactor for industrial wastewater treatment by quorum quenching. J Memb Sci 690:. https://doi.org/10.1016/j.memsci.2023.122198

1